Multiscale approach to predict strength of notched composite plates

Lucas L. Vignoli [a,b], Marcelo A. Savi [a], Pedro M.C.L. Pacheco [c], Alexander L. Kalamkarov [d,*]

[a] *Center for Nonlinear Mechanics, COPPE – Department of Mechanical Engineering, Universidade Federal do Rio de Janeiro, Rio de Janeiro, RJ, Brazil*
[b] *Center for Technology and Application of Composite Materials, Department of Mechanical Engineering, Universidade Federal do Rio de Janeiro, Macaé, RJ, Brazil*
[c] *Department of Mechanical Engineering, Centro Federal de Educação Tecnológica Celso Suckow da Fonseca CEFET/RJ, Rio de Janeiro, RJ, Brazil*
[d] *Department of Mechanical Engineering, Dalhousie University, Halifax, Nova Scotia B3H 4R2, Canada*

ARTICLE INFO

ABSTRACT

Success in design and application of composite materials to a large extend depends on the use of the adequate strength and failure criteria. The World-Wide Failure Exercise (WWFE) is an international effort to establish recommendations on failure criteria for the composite materials. WWFE uses the macromechanical approach and considers the effective (averaged) properties of laminae as input in the analysis. Therefore, a prior fundamental issue arises on which micromechanical approach is better to apply to calculate the effective properties of laminae. The objective of this paper is to present a multiscale analysis of influence of different micromechanical models on the damage onset in the notched composite laminates in comparison with the available experimental data. The failure modes of the CFRP and GFRP laminated plates with a circular hole subjected to tensile and compressive loads are analyzed. The WWFE recommendations are combined with different micromechanical approaches including a VSPK micromechanical model recently proposed by the authors. It is shown that the VSPK model presents better predictions for a broad range of experimental data compared with the other models available in the literature.

1. Introduction

Analysis and design of composite materials involves several variables in different scales, from micro to macro levels, see, e.g., [1,2]. Each composite characteristic requires application of the adequate micromechanical model. In this regard, there is an international effort that aims to guide composite design called World-Wide Failure Exercise (WWFE). This effort is now in the third edition [3] and the main results of the first and second editions of WWFE are summarized by Refs. [4] and [5], respectively.

In general, WWFE suggests composite design approaches, establishing a set of recommendations on which failure criterion provides the best prediction comparing with the experimental data in each case. The plane stress cases were selected in the first edition of WWFE, while 3D stress cases were included in the second stage. In the third edition of WWFE, some additional issues were evaluated, like matrix cracking evolution and notch effects. For all editions, the initial damage and the final failure modes are established and the matrix, fiber and the effective properties for each laminate are selected as input. Hence, even with the great contribution of WWFE guidelines, there is still a lack

of knowledge in the prior fundamental issue: the influence of the analytical micromechanical model capability to predict effective elastic properties and macromechanical strengths for the appropriate selection of fiber and matrix in the structural design. Note that laminae properties are provided by the WWFE's organizers, and for another lamina with the same fiber and matrix, but different fiber volume fraction, a new experimental testing must be carried out. The adequate micromechanical modeling is especially significant for the design optimization of composite structures, see [6].

Micromechanics is an important part in composite analysis and design, defining the macromechanical effective (averaged) properties based on fiber, matrix and interface properties. Literature presents several analytical micromechanical models to estimate these effective properties [1,6–10]. Most of them are restricted to elastic properties and usually are compared with a very small number of experimental data.

Considering the models related to three editions of WWFE, just a few of them consider micromechanics aspects and, usually, they employ only numerical tools [11]. Carrere et al. [11] suggested that multiscale finite element model is useful approach to investigate com-

posite structures, allowing the inclusion of nonlinear effects. An alternative numerical approach is proposed by Ref. [12]. Nevertheless, this approach has high computational costs, especially due to the need of huge parametric analysis and mesh size. Based on that, the use of analytical models is an important approach. In this regard, the analytical approaches should be highlighted, like the Chamis model [13] and Bridging model [14]. An extensive discussion about the advantage of analytical modelling is presented by Ref. [15].

Composite structures usually have complex geometries and variable types of loading. And that complicates the failure analysis. Commonly, damage is initiated in the vicinity of abrupt variations in geometry, for example, around notches or holes. There are few analytical efforts to analyze the influence of macromechanical stress concentration near the notches in composite materials. For stress concentration problems in anisotropic materials the main contributions are presented in [16–20]. But all of them are limited to determine the stress distribution around holes and no investigation is presented on damage initiation or propagation. In this regard, the analytical failure model for composite plates with holes proposed by Ref. [21] should be noted. It assumes that under the uniaxial load, failure is initiated in the same location as for the isotropic plates. Nevertheless, experimental work in [22] and theoretical study in [23] demonstrate that the maximum stress concentration in composites is not always at the same point as in isotropic homogeneous materials and, in addition, the failure may not be initiated at the maximum stress concentration.

Refs. [24,25] employed Moiré interferometric technique to experimentally measure strain fields and to quantify damage around notches. Ref. [26] discussed the influence of specimen geometry. Ref. [27] presented a comparative experimental analysis of composites using carbon and glass fibers, evaluating the influence of fiber types on the failure mechanisms. As pointed out by Ref. [28], the conclusions from the experimental studies are quite limited because there is a large number of involved variables.

Ref. [29] presented analytical discussion about damage onset in large laminated plates with elliptical holes subjected to in-plane loads. A second part of this investigation is presented in Ref. [23] for circular holes and uniaxial (tension and compression) loads including damage propagation using the finite element simulations. The aim of this study is to proceed with this discussion including multiscale aspects on the design of notched unidirectional laminates. The novel micromechanical model VSPK is recently developed by the authors, see [30–32]. It is applied to analyze the influence of fibers on the damage onset in the CFRP and GFRP laminates. As pointed out in Ref. [15], the analytical approaches are fundamental tools for optimal design and the multiscale procedure proposed in the present paper allows estimating analytically the onset strength of a notched plate using the properties of constituent materials.

The adopted multiscale procedure is illustrated in the Fig. 1. Matrix, fiber and interface properties and volume fractions are the inputs in this analysis and the proposed micromechanical model is applied to determine the effective properties of the lamina assuming perfect bonding between the fibers and matrix. For a discussion about imperfect bonding see [33]. As consequence of this micromechanical approach, it is assumed that the heterogeneous plate is macroscopically equivalent to the homogeneous anisotropic plate for all fiber volume fractions, as illustrated in step 2. The homogenized plate with effective properties is considered in steps 2–4.

Three different coordinate systems are necessary to deal with the stress concentration problem: global coordinates, $x_i^{(g)}$, where the applied loads are defined and for this investigation the uniaxial load with $\sigma_{11}^{(g)} = \sigma_n$ and $\sigma_{22}^{(g)} = \sigma_{12}^{(g)} = 0$ is considered; material coordinates, x_i, where material properties are defined and x_1 coincides with the fiber orientation; and local coordinates, $x_i^{(l)}$, employed to map the border of the hole. The angle between x_1 and $x_1^{(l)}$ is θ and angle between x_1

and $x_1^{(g)}$ is α. σ_n denotes the nominal stress applied on the plate in a region far enough from the hole to disregard border effects and to be assumed infinity.

In Section 2, the VSPK micromechanical model is presented in full details. In Section 3, the Stroh formalism is introduced, and the main equation to compute the stress distribution along the hole border is highlighted. Section 4 presents the Puck failure criterion to properly define damage initiation following the WWFE recommendation for failure of composite plates. Finally, in Section 5 all these steps are coupled to evaluate the influence of fiber volume fraction, fiber-to-load angle and fiber types on damage onset in notched composites. For simplicity, henceforth notched strength is used to denote the applied load that results on damage onset in a notched composite plate.

2. VSPK micromechanical model

The micromechanical model VSPK used in this study was recently proposed in [30–32]. For the elastic properties, the rule of mixture equations for longitudinal elastic modulus, E_1, and longitudinal Poisson's ratio, ν_{12}, results in a good estimation when compared with experimental data. On the other hand, for transversal elastic modulus, E_2, and longitudinal shear modulus, G_{12}, a modification of the rule of mixture is recommended to improve the model capability. Assuming a thin ply in plane stress condition, the following equations are used to estimate the elastic properties of lamina:

$$E_1 = V_f E_1^f + (1 - V_f)E^m \tag{1}$$

$$\nu_{12} = V_f \nu_{12}^f + (1 - V_f)\nu^m \tag{2}$$

$$E_2 = E^m \left(\frac{1}{1 + \xi_{E_2}[(E^m/E_2^f) - 1]V_f} \right) \tag{3}$$

$$G_{12} = G^m \left(\frac{1}{1 + \xi_{G_{12}}[(G^m/G_{12}^f) - 1]V_f} \right) \tag{4}$$

where V_f is the fiber volume fraction, E_1^f and E_2^f are the fiber longitudinal and transversal elastic moduli, ν_{12}^f is the fiber longitudinal Poisson's ratio, G_{12}^f the is fiber longitudinal shear modulus, E^m is the matrix elastic modulus, ν^m is the matrix Poisson's ratio, $G^m = E^m/2(1 + \nu^m)$ is the matrix shear modulus and ξ_{E_2} and $\xi_{G_{12}}$ are calibrated functions defined by
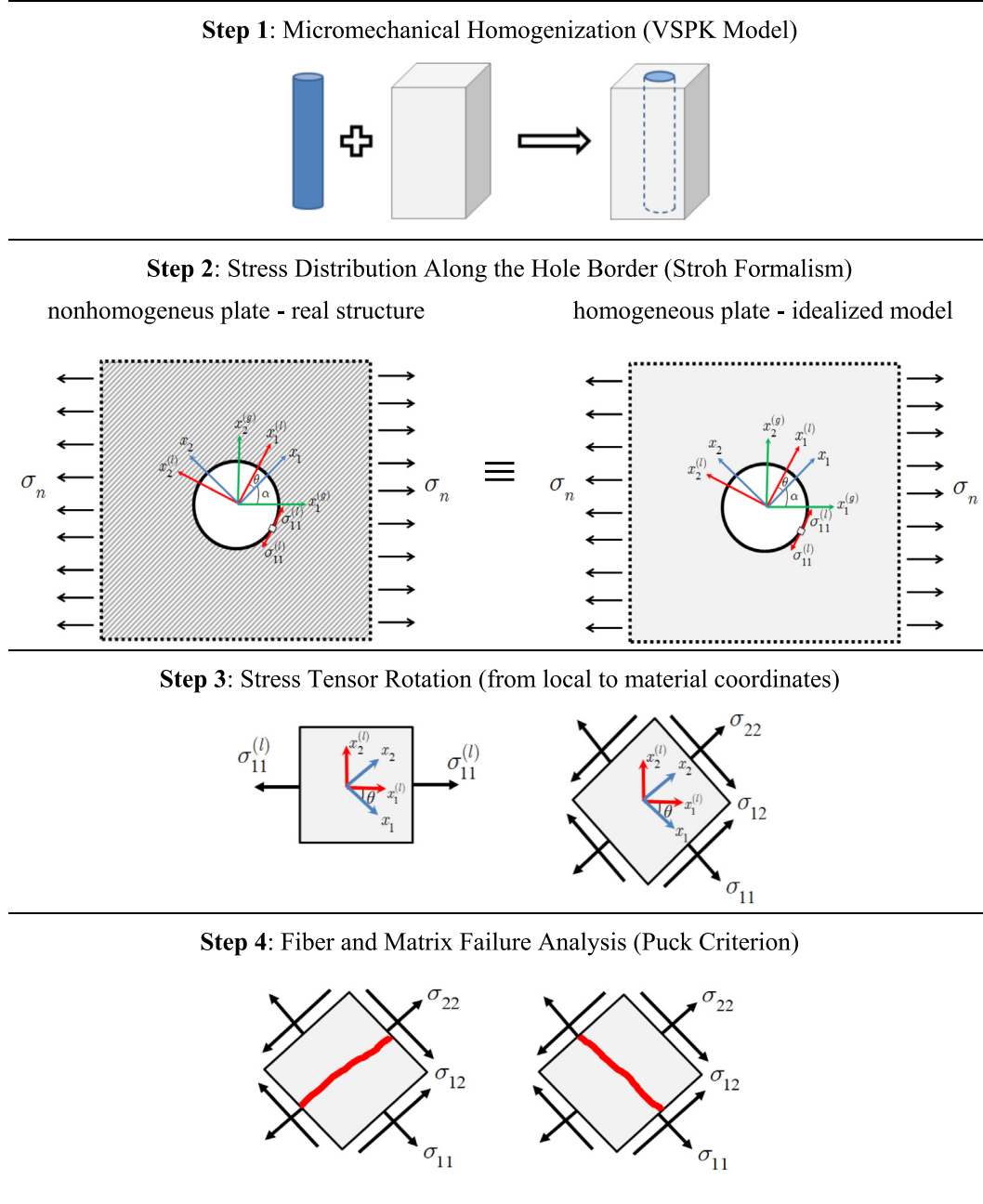
$$\xi_{E_2} = \left[a_1 + a_2 V_f + a_3(E^m/E_2^f) \right] \tag{5}$$

$$\xi_{G_{12}} = \left[a_4 + a_5 V_f + a_6(G^m/G_{12}^f) \right] \tag{6}$$

where a_i are calibrated according to the experimental data. Note that $\xi_{E_2} = 1$ and $\xi_{G_{12}} = 1$ for the traditional rule of mixture. Based on a set of 100 experimental data compiled from literature for CFRP and GFRP, with 54 data for E_2 and 46 data for G_{12}, the calibrated parameters are listed in the Table 1. Note that defining $\xi_{E_2} = 1$ and $\xi_{G_{12}} = 1$, Eq. (3) and (4) are the classical rule of mixture equations.

In summary, the following assumption are made for the strength evaluation:

(i) the rule of mixture estimation for longitudinal strengths has a good agreement with experimental data, however it can be improved including fiber *in situ* strength reduction induced by imperfections for longitudinal tensile strength, S_{11}^t;

(ii) for longitudinal compressive strength, S_{11}^c, the misaligned fiber is assumed to have a cubic polynomial shape and Castigliano's theorem is applied to relate the macroscopic load with the effective load on the fiber that results is crushing/rupture;

Step 1: Micromechanical Homogenization (VSPK Model)

Step 2: Stress Distribution Along the Hole Border (Stroh Formalism)

nonhomogeneus plate - real structure   homogeneous plate - idealized model

Step 3: Stress Tensor Rotation (from local to material coordinates)

Step 4: Fiber and Matrix Failure Analysis (Puck Criterion)

Fig. 1. Schematic view of the multiscale approach: the homogenization process is applied in the Step 1; and plate is assumed homogeneous and anisotropic in all consequent steps.

Table 1
Calibrated parameters to estimate effective elastic properties.

a_1	a_2	a_3
2.2603	-1.4759	-0.2964
a_4	a_5	a_6
2.3145	-1.6043	-0.4199

(iii) despite high nonlinear response of unidirectional laminae under longitudinal shear, concentric cylinder model estimation is used for the prediction of the longitudinal shear strength, S_{12}^s, assuming damage onset (associated with the start of the nonlinear region in an experimental shear stress–strain curve);

(iv) transversal strengths are derived considering elasticity-based analytical solution for inclusions in infinite medium and later calibrated for actual values of fiber volume fractions using finite element simulation; the transversal tensile strength, S_{22}^t, assumes failure by cavitation due to dilatational energy density while transversal compressive strength, S_{22}^c, considers failure on the interface.

Based on the above assumptions, the following closed-form equations are derived to estimate macromechanical strengths of unidirectional lamina:

$$S_{11}^t = \left[V_f + (1 - V_f)\left(\frac{E^m}{E_1^f}\right) \right](1 - r)S_t^f \tag{7}$$

$$S_{11}^c = \left[V_f + \left(\frac{E^m}{E_1^f} \right)(1 - V_f) \right] \left[\frac{1 + (272/315)(L\phi/d_f)^2}{1 + (8/3)(L\phi/d_f)} \right] S_c^f \tag{8}$$

$$S_{12}^s = \frac{S_s^m}{2} \left[\frac{(G_{12}^f + G^m) + (G_{12}^f - G^m)V_f}{G_{12}^f} \right] \tag{9}$$

$$S_{22}^t = \frac{1}{(1 + \nu^m)(1 - 2\beta)g_t(V_f)} \sqrt{\left(\frac{6E^m}{1 - 2\nu^m} \right) u_v^c} \tag{10}$$

$$S_{22}^c = \frac{S^i}{\sqrt{g_{ic}(V_f)}} \left(\frac{2}{1 - \beta} \right) \tag{11}$$

where S_t^f and S_c^f are the fiber tensile and compressive strengths, S_s^m is the matrix shear strength, u_v^c is the matrix critical dilatation energy density and S^i is the interface strength. r is the fiber strength reduction parameter, created based in experimental reports that fiber tensile strength measured in single fibers is smaller than *in situ* values [34]. For longitudinal compressive strength, a misaligned fiber geometry is considered with maximum misalignment angle and length ϕ and L, respectively, and fiber diameter d_f. For transversal strengths, the former equations are based on the stress solution of a single fiber embedded in an infinite matrix; *i.e.*, $V_f \to 0$ and any interaction between neighbor fibers is disregarded. To extend this formulation for real laminae, $g_t(V_f)$ and $g_{ic}(V_f)$ are functions created to include the influence of fiber volume fraction. These functions are calibrated using finite element simulations considering carbon and glass fibers in an epoxy matrix with $V_f = 0.3, 0.4, 0.5, 0.6, 0.7$ and the following equations are obtained:

$$g_t(V_f) = 1 - 5.8\gamma V_f^3 \tag{12}$$

$$g_{ic}(V_f) = -7.71(0.14 + \beta)V_f^3 + 6.63(0.01 + \beta)V_f^2 + 0.16(3 + \beta)V_f - 0.76(-0.24 + \beta) \tag{13}$$

where

$$\alpha = \frac{G^m \kappa^f - G_{23}^f \kappa^m}{G_{23}^f + G^m \kappa^f} \tag{14}$$

$$\beta = \frac{G^m - G_{23}^f}{G^m + G_{23}^f \kappa^m} \tag{15}$$

$$\gamma = \frac{\alpha - \beta}{(1 - \beta) - \beta(1 - \alpha)} \tag{16}$$

$$\kappa^m = 3 - 4\nu^m \tag{17}$$

$$\kappa^f = 3 - 4\nu_{23}^f \tag{18}$$

Here G_{23}^f is the fiber transversal shear modulus and $\nu_{23}^f = (E_2^f/2G_{23}^f) - 1$ is the fiber transversal Poisson's ration.

The following set of experimental data is compiled from literature for calibration: 27 data for S_{11}^t, 61 data for S_{11}^c, 31 data for S_{22}^t, 18 data for S_{22}^c. The calibrated parameters are: $r = 0.08$, $L\phi/d_f = 0.09$ or $L\phi/d_f = 2.39$, $u_v^c = 0.18MPa$ and $S^i = 65MPa$. Note that these are average values useful for general carbon and glass laminae, but they also can be calibrated for any laminae if experimental values are available. Additionally, for S_{11}^c, $L\phi/d_f = 0.09$ or $L\phi/d_f = 2.39$ have a very close estimation and replacing in Eq. (8), S_{11}^c can be estimated using the simple equation

$$S_{11}^c = \left[V_f + \left(\frac{E^m}{E_1^f} \right)(1 - V_f) \right] 0.8S_c^f \tag{19}$$

3. Analysis of stress concentration

Stroh formalism [19,20] is a mathematical formulation that is useful for the anisotropic elasticity due to its powerful capabilities and compact solutions when compared to other analytical approaches, e.g., Lekhnitskii formalism [17].

Considering linear elasticity, the equilibrium equation in the absence of body forces is written as follows:

$$c_{ijkl}u_{k,lj} = 0 \tag{20}$$

where c_{ijkl} is the elastic tensor and u_k is the displacement vector.

The general solution of this set of equations is $u = vg(z)$, or $u_k = v_k g(z)$, where v depends on the material properties, namely material eigenvectors, and $g(z)$ satisfies boundary conditions. In this expression, $z = x_1 + px_2$, where p is named material eigenvalue. The essential point of the Stroh formalism is the material eigenvalue equation:

$$[c_{i1k1} + (c_{i1k2} + c_{i2k1})p + c_{i2k2}p^2]v_k = 0 \tag{21}$$

By defining 3×3 matrices $\mathbf{Q}$, $\mathbf{R}$ and $\mathbf{T}$ in such a way that $Q_{ik} = c_{i1k1}$, $R_{ik} = c_{i1k2}$ and $T_{ik} = c_{i2k2}$, Eq. (21) can be rewritten in the matrix notations as follows:

$$\left[\mathbf{Q} + (\mathbf{R} + \mathbf{R}^T)p + \mathbf{T}p^2 \right]v = \mathbf{0} \tag{22}$$

After some algebraic manipulations, Eq. (22) can be redefined as a classical eigenvalue problem, being the basis of the Stroh formalism. For a detailed discussion about this derivation, see [19,20].

Since stress concentration problems around holes are related to the free surface, $\sigma_{11}^{(l)}$ is the only non-zero stress component along the border of the hole. Due to that, the local coordinate system is convenient for the problem solution and the following quantities need to be transformed from material coordinates:

$$\mathbf{Q}^{(l)} = \mathbf{Q}\cos^2\theta + (\mathbf{R} + \mathbf{R}^T)\sin\theta\cos\theta + \mathbf{T}\sin^2\theta \tag{23}$$

$$\mathbf{R}^{(l)} = \mathbf{R}\cos^2\theta + (\mathbf{T} - \mathbf{Q})\sin\theta\cos\theta + \mathbf{R}^T\sin^2\theta \tag{24}$$

$$\mathbf{T}^{(l)} = \mathbf{T}\cos^2\theta - (\mathbf{R} + \mathbf{R}^T)\sin\theta\cos\theta + \mathbf{Q}\sin^2\theta \tag{25}$$

The Stroh formalism has other additional quantities as the Barnett-Lothe second-order tensors. The non-zero components of which are expressed as follows considering orthotropic plates under plane stress:

$$[S_{BL}]_{12} = -(1 - \sqrt{\nu_{12}\nu_{21}}) \left[\left(\frac{E_1}{G_{12}} \right) + 2(1 - \sqrt{\nu_{12}\nu_{21}})\sqrt{\frac{E_1}{E_2}} \right]^{-1/2} \tag{26}$$

$$[S_{BL}]_{21} = (1 - \sqrt{\nu_{12}\nu_{21}}) \left[\left(\frac{E_2}{G_{12}} \right) + 2(1 - \sqrt{\nu_{12}\nu_{21}})\sqrt{\frac{E_2}{E_1}} \right]^{-1/2} \tag{27}$$

$$[L_{BL}]_{11} = E_1 \left[\left(\frac{E_1}{G_{12}} \right) + 2(1 - \sqrt{\nu_{12}\nu_{21}})\sqrt{\frac{E_1}{E_2}} \right]^{-1/2} \tag{28}$$

$$[L_{BL}]_{22} = E_2 \left[\left(\frac{E_2}{G_{12}} \right) + 2(1 - \sqrt{\nu_{12}\nu_{21}})\sqrt{\frac{E_2}{E_1}} \right]^{-1/2} \tag{29}$$

$$[L_{BL}]_{33} = \sqrt{G_{13}G_{23}} \tag{30}$$

Using the previously defined quantities, the solution of the normal stress distribution in local coordinates along the border of the hole can be written as follows:

$$\sigma_{11}^{(l)} = i_1(\mathbf{G}_1^{(l)}\tau_2 + \mathbf{G}_3^{(l)}\tau_2) - i_2(\mathbf{G}_1^{(l)}\tau_1 - \mathbf{G}_3^{(l)}\tau_2) \tag{31}$$

where $i_1 = [1 \ 0 \ 0]$ and $i_2 = [0 \ 1 \ 0]$, $\tau_1 = [\sigma_{11}^\infty \ \sigma_{12}^\infty \ 0]^T$ and $\tau_2 = [\sigma_{12}^\infty \ \sigma_{22}^\infty \ 0]^T$ define the applied load, σ_{ij}^∞ are the stress components in material coordinates far away from the hole, $\mathbf{G}_1^{(l)} = [\mathbf{N}_1^{(l)}]^T - \mathbf{N}_3^{(l)}\mathbf{S}\mathbf{L}^{-1}$ and $\mathbf{G}_3^{(l)} = -\mathbf{N}_3^{(l)}\mathbf{L}^{-1}$ are defined using a compact expression, where $\mathbf{N}_1^{(l)} = -[\mathbf{T}^{(l)}]^{-1}[\mathbf{R}^{(l)}]^T$ and $\mathbf{N}_3^{(l)} = -\mathbf{R}^{(l)}[\mathbf{T}^{(l)}]^{-1}[\mathbf{R}^{(l)}]^T - \mathbf{Q}^{(l)}$ are the fundamental elastic matrices. Using the normal stress in the local coordinates, the stress concentration along the notch border is defined by

$\sigma_{11}^{(l)}/\sigma_n$. Note that stress concentration is used hereafter in a macroscopic analysis.

Stress components σ_{ij}^{∞} are computed considering uniaxial load (see Fig. 1) using the following expressions:

$$\sigma_{11}^{\infty} = \frac{\sigma_n}{2}(1 + \cos 2\alpha) \tag{32}$$

$$\sigma_{22}^{\infty} = \frac{\sigma_n}{2}(1 - \cos 2\alpha) \tag{33}$$

$$\sigma_{12}^{\infty} = -\frac{\sigma_n}{2}\sin 2\alpha \tag{34}$$

4. Puck failure criterion

Simultaneous damage mechanisms make the prediction of failure in composite material a hard task. Therefore, WWFE presented several efforts to improve the failure criteria. Based on WWFE recommendations [4,5], Puck failure criterion [35] has been selected. This model has the advantage of the use of closed-expressions for the plane stress conditions and it is able to distinguish fiber and matrix failure.

The idea is to define failure functions for both constituents, as two independent failure mechanisms, and evaluate which one is the most critical. The failure function rises from zero to one. And it is assumed that failure takes place when the function is equal to one. In the sequence, these functions are defined according to the load condition.

Fiber failure is an essential point for composite material design. Usually, its modeling is based on the maximum stress theory. Nevertheless, there are two additional factors to be considered: the difference between Poisson's ratio of the composite constituents and the shear influence of the fiber instability during compression. Expressions of fiber failure during tension and compression are given, respectively, by

$$f_P^{(f,t)} = \frac{1}{S_{11}^t}\left|\sigma_{11} + \left(\frac{E_1}{E_1^f}\nu_{12}^f m_f - \nu_{12}\right)\sigma_{22}\right| \tag{35}$$

$$f_P^{(f,c)} = \frac{1}{S_{11}^c}\left|\sigma_{11} + \left(\frac{E_1}{E_1^f}\nu_{12}^f m_f - \nu_{12}\right)\sigma_{22}\right| + \left(10\frac{\sigma_{12}}{G_{12}}\right)^2 \tag{36}$$

where m_f is a parameter calibrated to fit experimental data.

Concerning matrix failure, critical plane concept from the Coulomb-Mohr failure criterion for brittle isotropic materials is adopted [36]. This concept allows defining the critical load as well as the failure direction, as illustrated in the Fig. 2. Assuming plane stress hypothesis, there exist three different failure modes (see Fig. 2). If $\sigma_{22} \geqslant 0$, mode A is the unique failure mode possible and the failure mechanism develops in a critical plane perpendicular to σ_{22}. If $\sigma_{22} < 0$ two different critical planes are possible: mode B is associated with a critical plane perpendicular to σ_{22} and mode C is related to a critical plane that has an inclination γ with respect to σ_{22}. Note that mode B takes place for smaller absolute values of σ_{22} than with mode C. For pure compression, material fails in mode C.
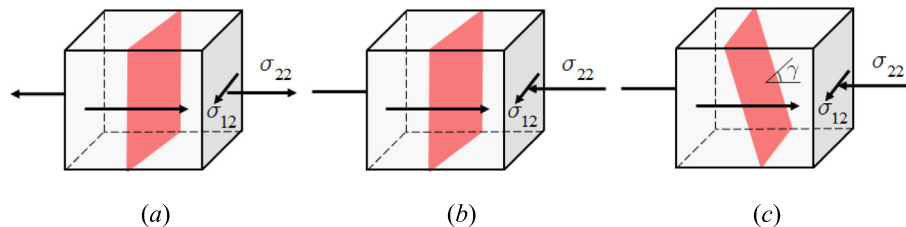
Adding the effect of voids and cracks growth due to $\sigma_{11} \neq 0$ in the Coulomb-Mohr-based failure criterion, matrix failure functions associated to the three failure modes are defined as follows:

$$f_P^{(m,A)} = \left(\frac{\sigma_{12}}{S_{12}}\right)^2 + \left(\frac{\sigma_{22}}{S_{22}^t}\right)^2 + 2\frac{p_{12}^t}{S_{12}}\sigma_{22}\left(1 - \frac{\sigma_{22}}{S_{22}^t}\right) + \left(\frac{\sigma_{11}}{X_{11}}\right)^n \tag{37}$$

$$f_P^{(m,B)} = \left(\frac{\sigma_{12}}{S_{12}}\right)^2 + 2\frac{p_{12}^c}{S_{12}}\sigma_{22} + \left(\frac{\sigma_{11}}{X_{11}}\right)^n \tag{38}$$

$$f_P^{(m,C)} = \left(\frac{\sigma_{12}\cos\gamma}{S_{12}}\right)^2 + \left(\frac{\sigma_{22}\sin\gamma\cos\gamma}{S_{23}^{(23)}}\right)^2 + 2\frac{p_{12}^c}{S_{12}}\sigma_{22}\cos^2\gamma + \left(\frac{\sigma_{11}}{X_{11}}\right)^n \tag{39}$$

where p_{12}^c and p_{12}^t are adjustable parameters; $X_{11} = 1.1S_{11}^t$ if $\sigma_{11} > 0$ or $X_{11} = -1.1S_{11}^c$ if $\sigma_{11} < 0$; it is assumed that parameter $n = 8$ and its physical meaning is to represent the influence of matrix cracking damage for higher normal stress parallel to the fibers' direction [35] and

$$\gamma = a\cos\left\{\sqrt{\frac{1}{2(1 + p_{12}^c)}\left[\left(\frac{S_{23}^{(23)}\sigma_{12}}{S_{12}\sigma_{22}}\right)^2 + 1\right]}\right\} \tag{40}$$

$$S_{23}^{(23)} = \frac{S_{12}}{2p_{12}^c}\left(\sqrt{1 + 2p_{12}^c\frac{S_{22}^c}{S_{12}}} - 1\right) \tag{41}$$

Note that the present study is devoted to analysis of notch effects in unidirectional laminae or a single-layered laminate, where all the laminae have the same orientation. Therefore, delamination failure is not a critical mechanism and it is disregarded.

5. Results and discussion

A parametric analysis of fiber influence in notched strength of laminated plates is presented below. Three different conditions are evaluated: fiber type (carbon or glass), fiber volume fraction and fiber orientation. First, the validation of the micromechanical model and the Stroh formalism is introduced.

5.1. Micromechanical model influence

The proposed micromechanical VSPK model for the effective elastic properties is extensively discussed in Ref. [30]. The goal of this Section is to present a brief overview of this model. In summary, the analytical models are compared with a set of 309 experimental data compiled from literature and the average errors of analytical micromechanical models are evaluated. For a comparison with other analytical models from literature, the Chamis and Bridging models are used. The equations of Chamis and Bridging models are presented in the Appendices A and B respectively.

Fig. 3 shows the average error of each model for all properties of lamina. Note that two different shear strengths are used: onset shear strength, $S_{12}^{s,o}$, that is the first damage event, which is assumed to coincide with the initial nonlinear behavior in experimental stress–strain
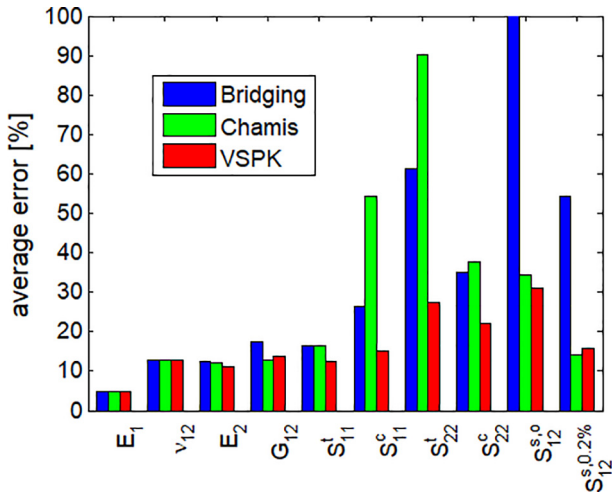

Fig. 2. Matrix failure mechanisms: (a) mode A, (b) mode B and (c) mode C.

Fig. 3. Average error of micromechanical models compared with 309 experimental data.

curves and offset shear strength, $S_{12}^{s,0.2\%}$, that is similar to yield strength for metals, being defined by the point where a line parallel to the shear modulus, but offset 0.2% on the strain axis, cross the stress–strain

curve. The first one is defined based on damage-free design and the second is defined by ASTM [37].

The application of the proposed VSPK model on the experimental data compiled from literature results on a smaller average error for almost all properties than Chamis and Bridging models. The exceptions are G_{12} and $S_{12}^{s,0.2\%}$, where Chamis model obtained the smallest average error but the difference between Chamis and VSPK is smaller than 1%. Regarding VSPK model, just $S_{12}^{s,o}$ estimation has an average error higher than 30%. On the other hand, estimations by Chamis and Bridging models have errors higher than 60%.

The micromechanical model influence on the predicted parameters, for notched strength for tensile, $S_o^t(\alpha, V_f)$, and compressive loads, $S_o^c(\alpha, V_f)$, are presented in the Fig. 4 considering the fiber-to-load angle $\alpha = 90°$ and $0.3 \leqslant V_f \leqslant 0.7$. $\alpha = 90°$ is selected to illustrate this comparison, as for this condition $S_o^t(90°, V_f)$ and $S_o^c(90°, V_f)$ are directly influenced by lamina transversal strengths, S_{22}^t and S_{22}^c, which are presented in the Fig. 5.

Fig. 4 demonstrates that Chamis and Bridging models estimate higher values for $S_o^t(\alpha, V_f)$ than the VSPK model for the evaluated fiber volume fraction range. On the other hand, for $S_o^c(90°, V_f)$ there exist an oposite tendency; Chamis and Bridging models underestimate $S_o^c(90°, V_f)$ when compared with the VSPK model. Fig. 5 shows the results for S_{22}^t and S_{22}^c, where the same behvior is observed. A comparison between Figs. 4 and 5, shows that $S_o^t(90°, V_f)$ and S_{22}^t present similar behavior. The same is also observed for $S_o^c(90°, V_f)$ and S_{22}^c.

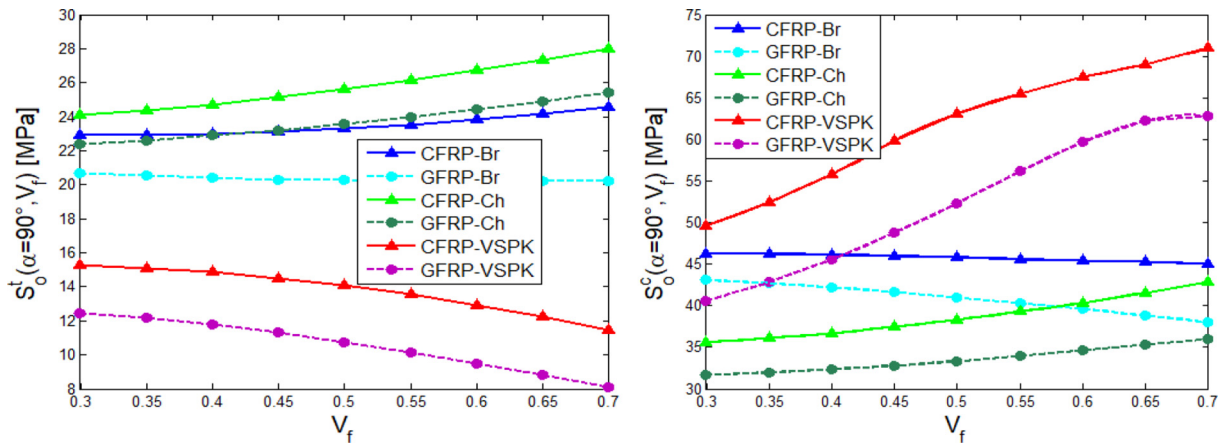**Fig. 4.** Comparison of damage onset for notched plates with $\alpha = 90°$, $S_o^t(90°, V_f)$ and $S_o^c(90°, V_f)$, using Bridging (Br), Chamis (Ch) and VSPK models.
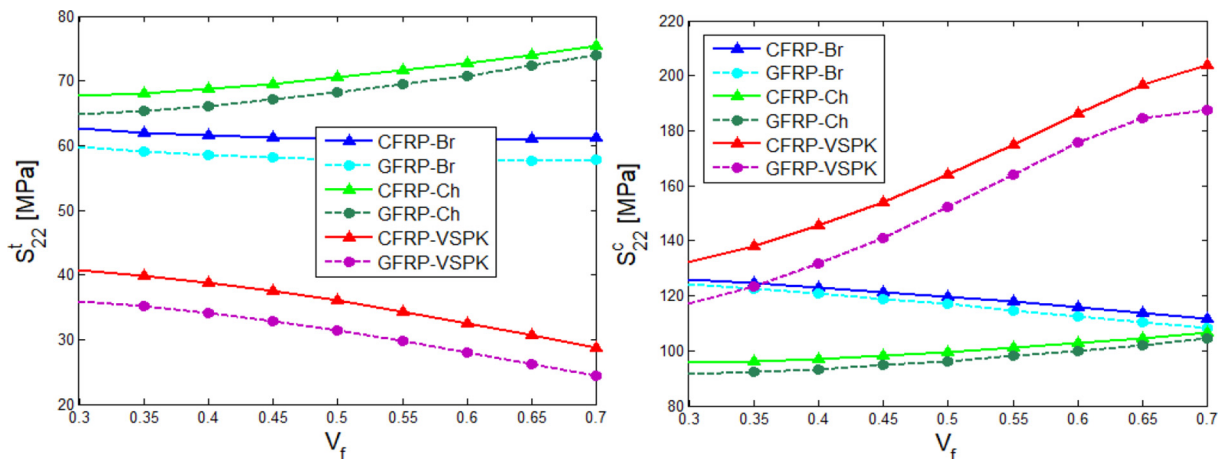

Fig. 5. Comparison of transversal strengths for unnotched, S_{22}^t and S_{22}^c, using Bridging (Br), Chamis (Ch) and VSPK models.

Based on the comparison of all three models with the compiled experimental data shown in the Fig. 3, the proposed VSPK model gives the best estimations for S_{22}^t and S_{22}^c. Due to the similarity between the transversal nocthed and unnotched strengths presented in Figs. 4 and 5, it is possible to conclude that Chamis and Bridging models may also overestimate $S_o^t(90°, V_f)$ and underestimate $S_o^c(90°, V_f)$.

5.2. Influence of plate dimensions

The objective of this Section is to evaluate the error associated with the assumption of an infinite plate in the analytical model based on the Stroh formalism. For a finite plate, the stress distribution is calculated by the finite element simulation using the commercial software ANSYS.

The constituents' properties are listed in Table 2. $V_f = 0.3$ and $V_f = 0.7$ are adopted as they are limiting values for the practical applications; and the fiber-to-load angles of $\alpha = 0°, 15°, 30°, 45°, 60°, 75°, 90°$ are considered. The VSPK micromechanical model is used to compute effective elastic properties for a CFRP and GFRP that are used as input in the finite element model.

Longitudinal dimension of plate is assumed to be 60 times larger than the hole diameter to avoid the border effects [39]; and transversal dimension of plate is assumed to be 6 times larger than the hole diameter to reproduce standard recommendations for the open-hole tests [40,41]. Assuming also that the laminate is under plane stress condition, the higher order element PLANE183 is used and an element discretization of 120 division around the hole border is adopted. Plate mesh is shown in the Fig. 6.

The maximum stress concentration variation vs. fiber-to-load angle α is shown in the Fig. 7 for both types of fibers and fiber volume fractions. The absolute error for the maximum stress concentration from the infinite plate assumption in the analytical solution is presented in the Fig. 8. These results indicate that Stroh formalism can be used with an error smaller than 10% for CFRP and smaller than 5% for GFRP.

5.3. Parametric study

The influence of three main factors are investigated below: the fiber type, volume fraction of constituents and fiber orientation. Among these parameters, only the fiber type is a discrete variable. Therefore, the analyses of CFRP and GFRP are carried out in parallel for comparison.

First, the stress concentration is analyzed. The influence of fiber volume fraction V_f is studied for $\alpha = 0°, 45°, 90°$, due to the common engineering application of the 10% rule [42], suggesting that a laminate is designed using only laminae with fiber orientations of $0°$, $+45°$, $-45°$ and $90°$; and that each lamina orientation should have at least 10% of the entire thickness of a laminate. Figs. 9 and 10 show the variation of stress concentration $\sigma_{11}^{(l)}/\sigma_n$ along the circular hole border θ for CFRP and GFRP, respectively. These results indicate that:

(i) the stress concentration is more severe for CFRP than for GFRP due to carbon fiber anisotropy;
(ii) the stress concentration is almost insensitive to the fiber volume fraction for $0.3 \leqslant V_f \leqslant 0.7$;
(iii) for CFRP the stress concentration ranges between -4.5 and 7.5 and for GFRP it ranges between -2.5 and 4. In comparison, for a large isotropic homogeneous plate with a circular hole subjected to uniaxial load the stress concentration ranges between -1 and 3, see Castro and Meggiolaro (2016).

Note that the negative values indicate that even for the applied tensile load there are some regions around the hole border under compression and vice-versa.

The influence of fiber-to-load angle on stress concentration along the hole border is shown in the Fig. 11 for $\alpha = 0°, 15°, 30°, 45°, 60°, 75°, 90°$ with a fixed fiber volume fraction $V_f = 0.5$. Thick black line in Fig. 11 indicates the circular hole border, the dashed black lines show the magnitudes of stress concentration and the color lines indicate the stress distribution for different values of α. Note that CFRP and GFRP have the same scale. It is possible to

Table 2
Matrix and fibers properties [38].

Matrix			Fiber		
	Epoxy (MY750)			Carbon (IM7)	Glass (E-glass)
E^m [GPa]	3.35		E_1^f [GPa]	276	74
ν^m	0.35		E_2^f [GPa]	19	74
S_t^m [MPa]	80		G_{12}^f [GPa]	27	30.8
S_c^m [MPa]	120		ν_{12}^f	0.2	0.2
			S_t^f [MPa]	5180	2150
			S_c^f [MPa]	3200	1450
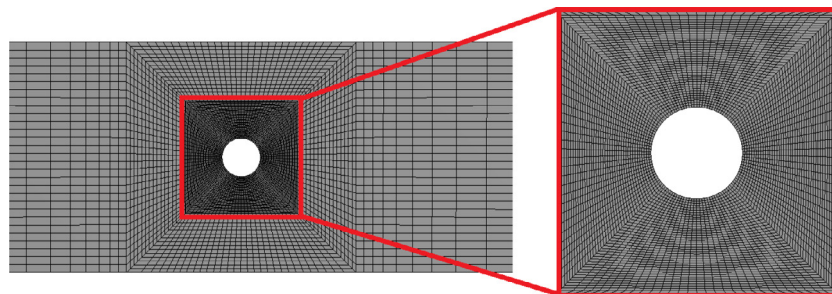
Fig. 6. Finite element mesh for a finite plate with a circular hole, and a zoom of the mesh near the hole.
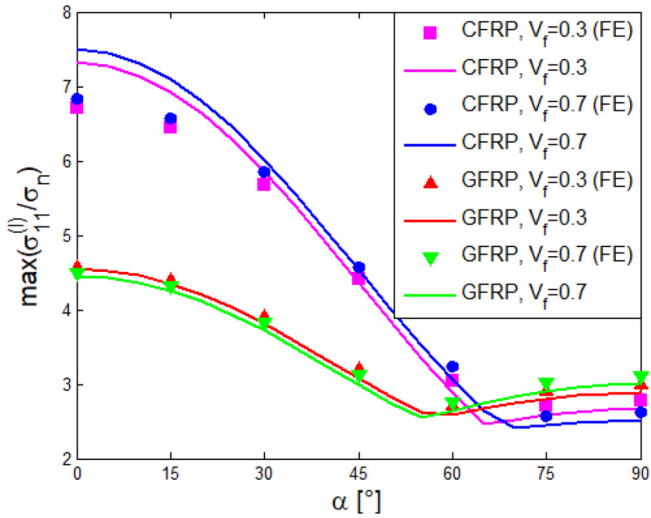
Fig. 7. Comparison between maximum stress concentration for infinite plates (analytical solution) and finite plates (finite element simulation).
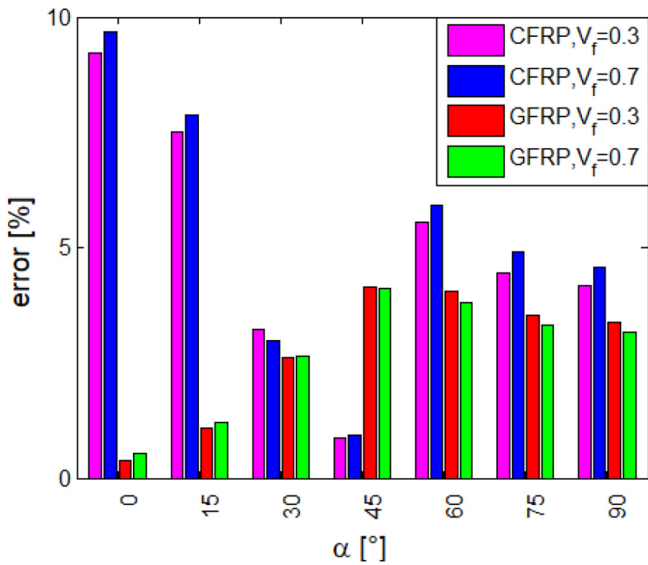

Fig. 8. Error on the maximum stress concentration from the infinite plate assumption.

conclude that the maximum stress concentration tends to occur in the point where the fiber orientation is tangent to the hole border.

Despite the stress concentration insensitivity in relation to V_f observed in Figs. 9 and 10, it is not possible to affirm that notch effects are insensitive to V_f in composite plates. The analysis of notch sensibility to V_f must also address the notch strength besides the stress concentration. Fig. 12 shows the notched tensile and compressive strengths vs. V_f for $\alpha = 0°, 45°, 90°$ using Puck parameters listed in the Table 3. Due to the absence of experimental data to calibrate these parameters, they are assumed to be independent of the fiber volume fraction. For a discussion on experimental issues related to the calibration of these parameters, see [36]. These results indicate that:

(i) despite that carbon fibers are twice stronger than glass fibers, the laminate notched strengths do not demonstrate this discrepancy;

(ii) all laminates indicate smooth variation of notched tensile strength, S_o^t vs. V_f. It increases for $\alpha = 0°$ and decreases for $\alpha = 45°, 90°$ with the increase of V_f;

(iii) for notched compressive strength, S_o^c, GFRP has an abrupt variation for $\alpha = 0°$;

(iv) for CFRP subjected to compressive load, notched strengths for $\alpha = 0°$ and $\alpha = 90°$ are virtually equal for $V_f > 0.5$;

(v) fiber orientation $\alpha = 45°$ has the smallest notched compressive strength for both fiber types;

(vi) in some cases increase of V_f results in decrease of strength for both fiber types, see, e.g., $S_o^c(\alpha = 0°, V_f)$ for GFRP with $V_f > 0.5$.

Figs. 13 and 14 show Puck's failure functions variation along the hole border for notched tensile strength, S_o^t, for the fiber-to-load angles $\alpha = 0°, 45°, 90°$ and fiber volume fraction $V_f = 0.5$. The matrix mode A failure under tension is observed for both, CFRP and GFRP. Despite that carbon fibers are twice stronger than glass fibers, the failure is determined by the matrix failure mechanism. Hence, despite the difference between tensile strengths of carbon and glass fibers, the difference between CFRP and GFRP tensile nocthed strengths is not so pronounced.

In order to analyze the notched compressive strength S_o^c, two critical cases are selected: CFRP with $\alpha = 90°$ (see Fig. 15) and GFRP with $\alpha = 0°$ (see Fig. 16).

Fig. 15 shows the failure mechanism change for CFRP. For small values of V_f, failure takes place in mode C and failure mechanism tends to change to mode B when $V_f \rightarrow 0.7$. The matrix is under compression for both failure modes, but the critical plane is different (see Fig. 2). On the other hand, for GFRP, Fig. 16 shows that there is a drastic change in the failure mode: for small values of V_f matrix fails in mode B (compression) and when V_f increases matrix tends to fail in mode A (tension). In other words, even under compressive load, matrix can fail under tension. This failure mechanism change is responsible for abrupt variation of $S_o^c(\alpha = 0°, V_f)$ presented in Fig. 12.

An alternative way to evaluate the failure modes is based on failure envelopes. Fig. 17 presents matrix failure envelopes in plane $\sigma_{12} - \sigma_{22}$ at the failure onset for CFRP with $\sigma_n = -S_o^c(\alpha = 90°, V_f)$ and GFRP with $\sigma_n = -S_o^c(\alpha = 90°, V_f)$. In the Fig. 17, green, blue and cyan lines indicate matrix failure modes A, B and C, respectively; and red triangles show the stress states along the hole border. On damage onset, one triangle must coincide with the failure envelope, what means that this stress state is resulting in matrix failure. Modes C and B are observed for CFRP and modes B and A for GFRP.

The parameters p_{12}^c and p_{12}^t are related to the tangent of the failure surface when $\sigma_{22} = 0$. As previously discussed, they are assumed independent of the fiber volume fraction. Despite this limitation of the present analysis, there is no experimental data to verify if these parameters are functions of V_f or not. Additionally, it is expected that even if p_{12}^c and p_{12}^t are dependent on V_f, they are limited in a small range and the estimated notched strength will not have significant variation.

Despite the practical advantage of discrete values of α, a considerable effort has been carried out recently to improve manufacturing processes to fabricate composites with any α, regarding a continuous range, based on optimum analysis [43]. Hence, α is assumed also a continuous variable as well as V_f. Figs. 18 and 19 show influences of α and V_f on S_o^t and S_o^c, in the range of $0° \leqslant \alpha \leqslant 90°$ and $0.3 \leqslant V_f \leqslant 0.7$.

Fig. 18 shows that S_o^t has a smooth variation, and CFRP has higher tensile strength than GFRP for any combination of α and V_f. Additionally, S_o^t is always maximized for $\alpha = 0°$; i.e., notched tensile strength is maximum for the maximum stress concentration condition (see Figs. 9–11). CFRP and GFRP also present similar results for S_o^c, as shown in Fig. 19, with the smallest strength close to $\alpha \cong 45°$.

Figs. 20 and 21 show the failure mechanism variation vs. α and V_f for tensile ($\sigma_n = S_o^t$) and compression ($\sigma_n = -S_o^c$) loadings applied to the notched plate, respectively.
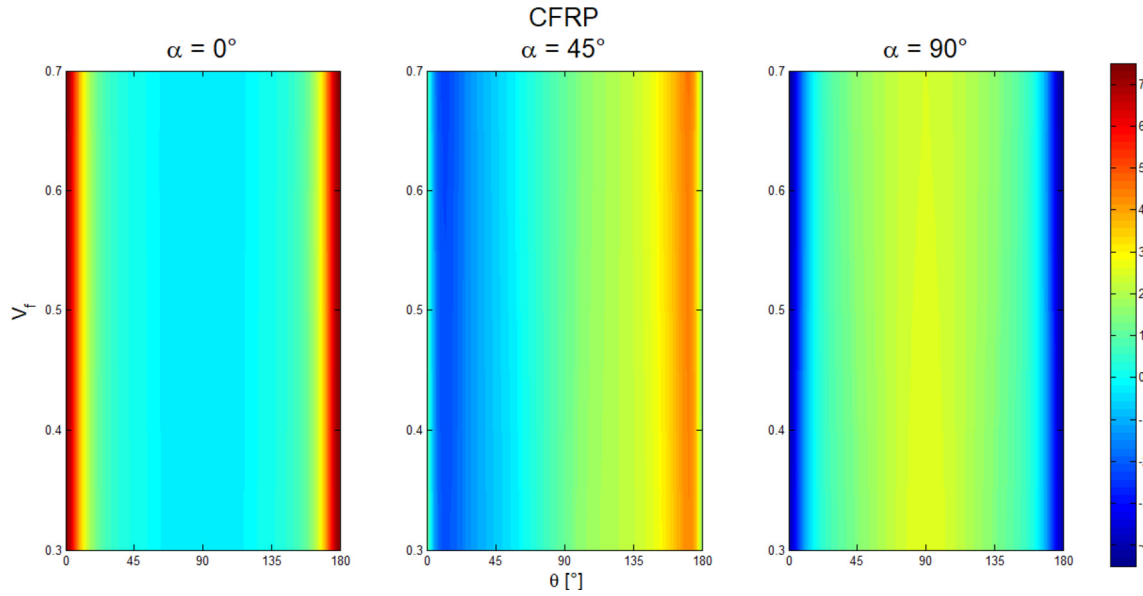
Fig. 9. Variation of stress concentration $\sigma_{11}^{(l)}/\sigma_n$ along the hole border for a large CFRP plate with a circular hole vs. V_f for $\alpha = 0°, 45°, 90°$.
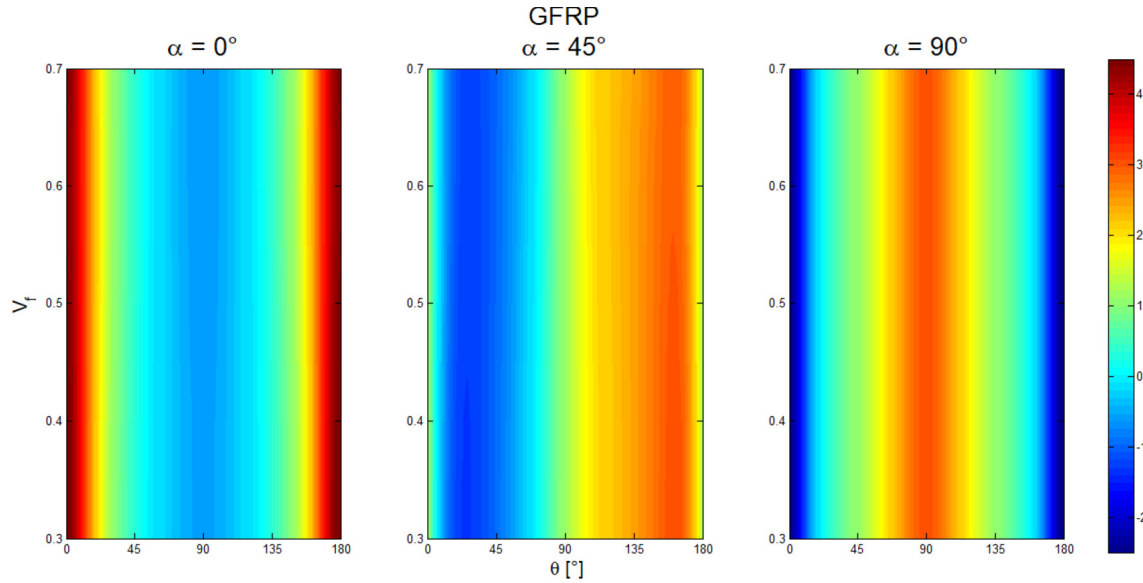

Fig. 10. Variation of stress concentration $\sigma_{11}^{(l)}/\sigma_n$ along the hole border for a large GFRP plate with a circular hole vs. V_f for $\alpha = 0°, 45°, 90°$.

In extension to the above discussion based on Figs. 13–16, the following conclusions can be made on the basis of results presented in the Figs. 18–21:

(i) for $\sigma_n = S_o^t$, there exists only one failure mode, namely mode A, where the matrix is under tension for both types of laminates;

(ii) for $\sigma_n = -S_o^c$, CFRP presents both matrix failure modes B and C under compression;

(iii) for $\sigma_n = -S_o^c$, GFRP presents both matrix failure modes under compression, namely modes B and C, as well as failure mode A, where the matrix is under tension.

Failure under tension of a plate subjected to compressive load has an important role for brittle isotropic materials. Griffith's classical study on micro-defects in brittle isotropic materials has estimated compressive strength to be 8 times higher than tensile strength [44,45].

However, for the composite materials this point is not yet analyzed and discussed as it deserves.

In a general sense, results show that the proposed by the authors VSPK micromechanical model can be efficiently implemented in the multiscale procedure, providing appropriate calculation of the effective properties required as input for the macromechanical analysis. In macromechanical modeling, the classical stress analysis formalism can be applied together with the WWFE's guidelines for failure definition. The proposal for the further development of multiscale analytical modeling is to evaluate the influence of V_f on the parameters p_{12}^c and p_{12}^t of the Puck failure criterion.

6. Conclusions

A multiscale analytical study is presented to evaluate the influence of the constituent properties of the composite laminates and
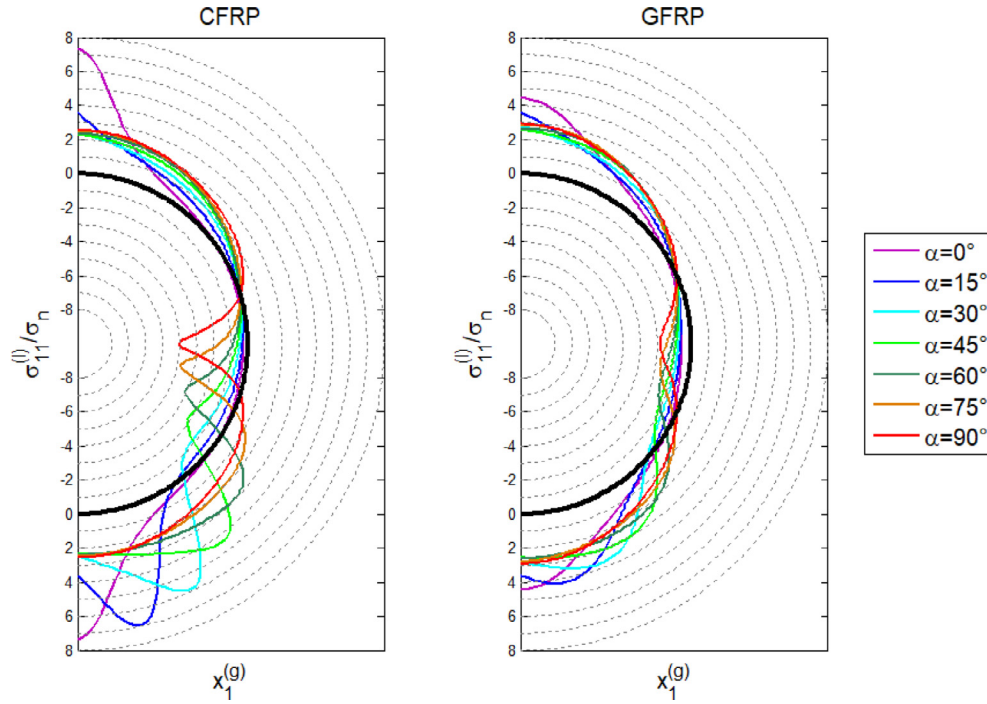
Fig. 11. Stress concentration for CFRP and GFRP for $V_f = 0.5$ and $\alpha = 0°, 15°, 30°, 45°, 60°, 75°, 90°$.

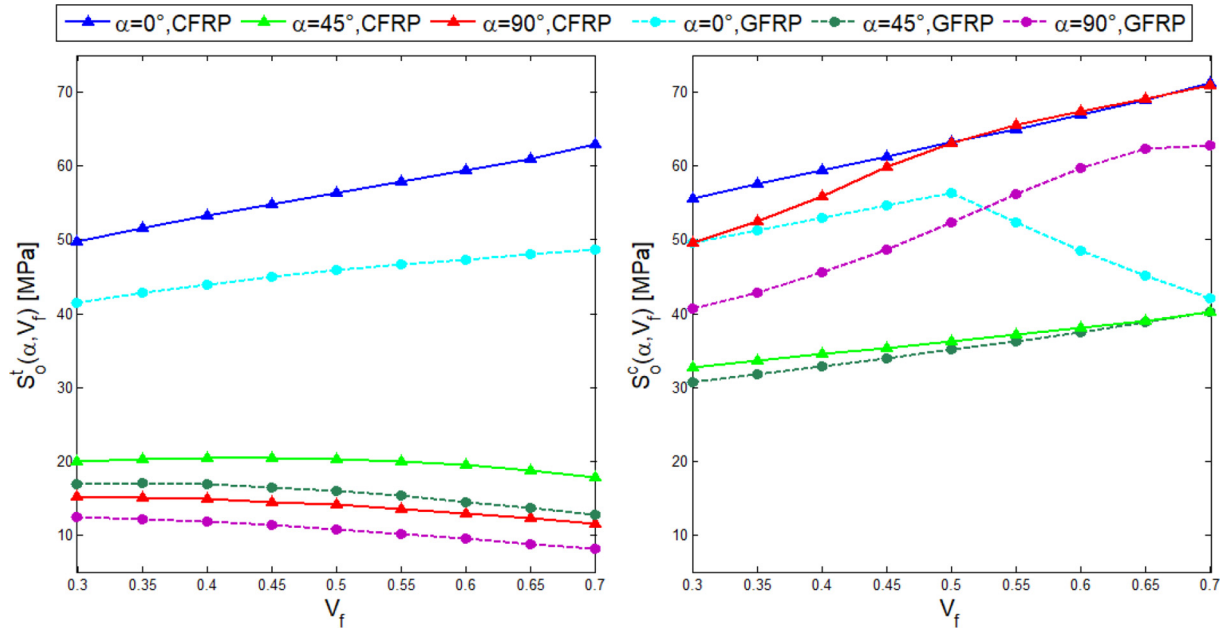**Fig. 12.** Tensile, S_o^t, and compressive, S_o^c, notched strengths vs. V_f for $\alpha = 0°, 45°, 90°$.

Table 3
Puck criterion parameters [35].

	p_{12}^c	p_{12}^t	m_f
CFRP	0.3	0.35	1.1
GFRP	0.25	0.3	1.3

the micromechanical models used to calculate their effective properties on the estimation of strength of notched unidirectional laminated plates. The CFRP and GFRP laminated plates with a circular

hole were considered in the analysis. The Chamis, Bridging equations and VSPK micromechanical model recently proposed by the authors [30–32] have been used to calculate the effective properties, estimate the notched strength and determine the failure modes of laminates. It is shown that the VSPK model provides better results compared with the other micromechanical models for a broad range of experimental data. Stress distribution along the hole border is obtained analytically using Stroh formalism and a comparison with finite element simulations for the finite plates indicates an error smaller than 10% due to assumption of an infinite plate in
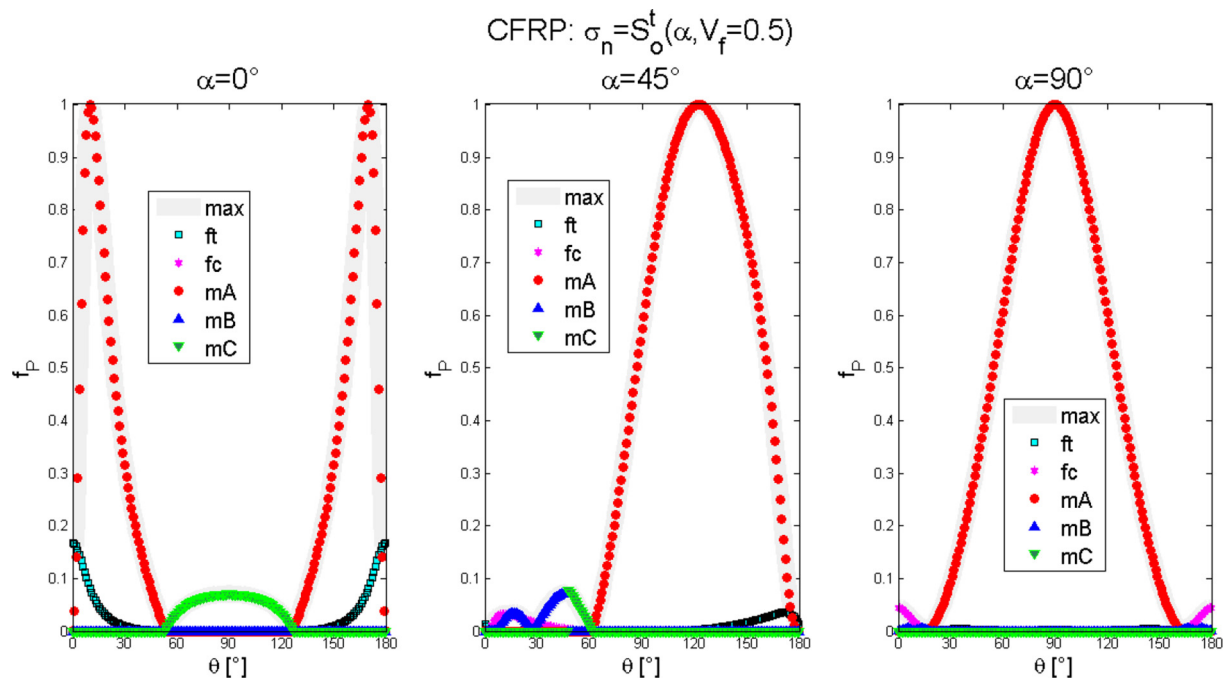
Fig. 13. Influences of fiber-to-load angle α on failure mode for CFRP with tensile load $\sigma_n = S_o^t(\alpha, V_f = 0.5)$.
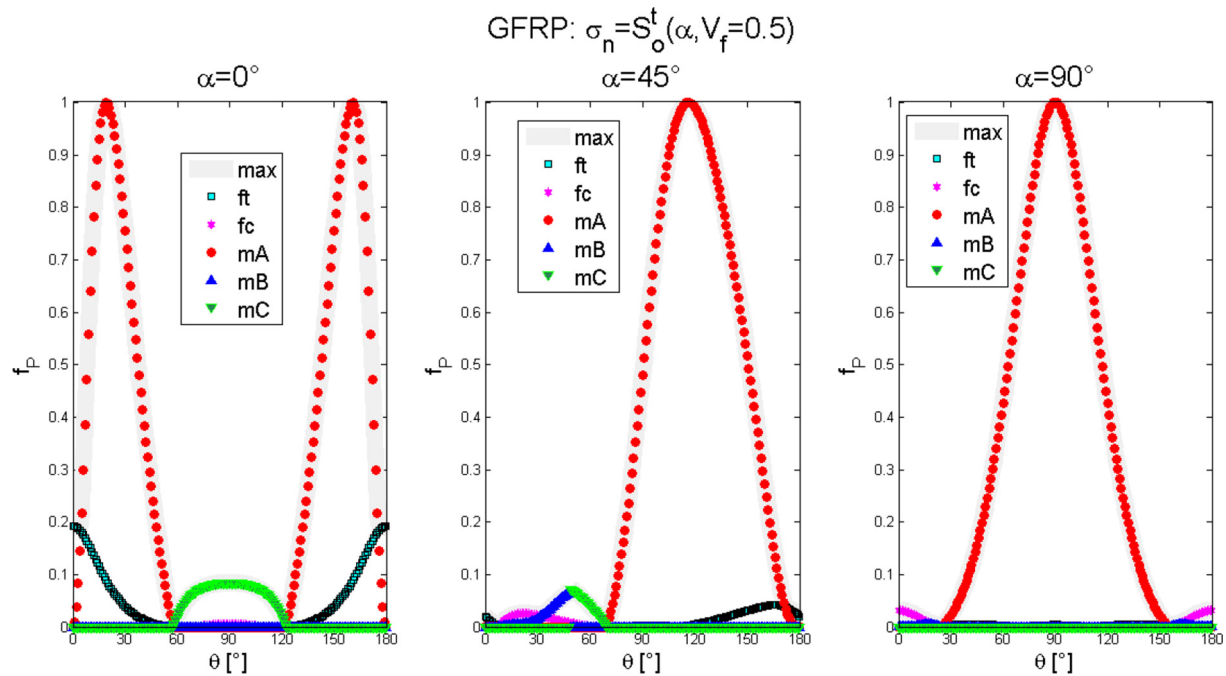

Fig. 14. Influences of fiber-to-load angle α on failure mode for GFRP with tensile load $\sigma_n = S_o^t(\alpha, V_f = 0.5)$.

analytical solution. Based on the WWFE recommendations the Puck failure criterion is selected for the damage analysis. The matrix failure was observed for the tensile and compressive loads. For tensile load, matrix fails under tension (mode A) around the hole border. For compressive load, matrix fails under compression in modes B and C for CFRP around the notch while for GFRP the matrix also fails in mode A. Therefore, even for the compressive load the matrix may fail under tension. The presence of this failure mode in GFRP is associated with an abrupt variation in notched compressive strength $S_o^c(\alpha, V_f)$ for fiber-to-load angle $\alpha = 0°$ with fiber volume fraction V_f larger than 0.5.

Declaration of Competing Interest

The authors declare that they have no known competing financial interests or personal relationships that could have appeared to influence the work reported in this paper.
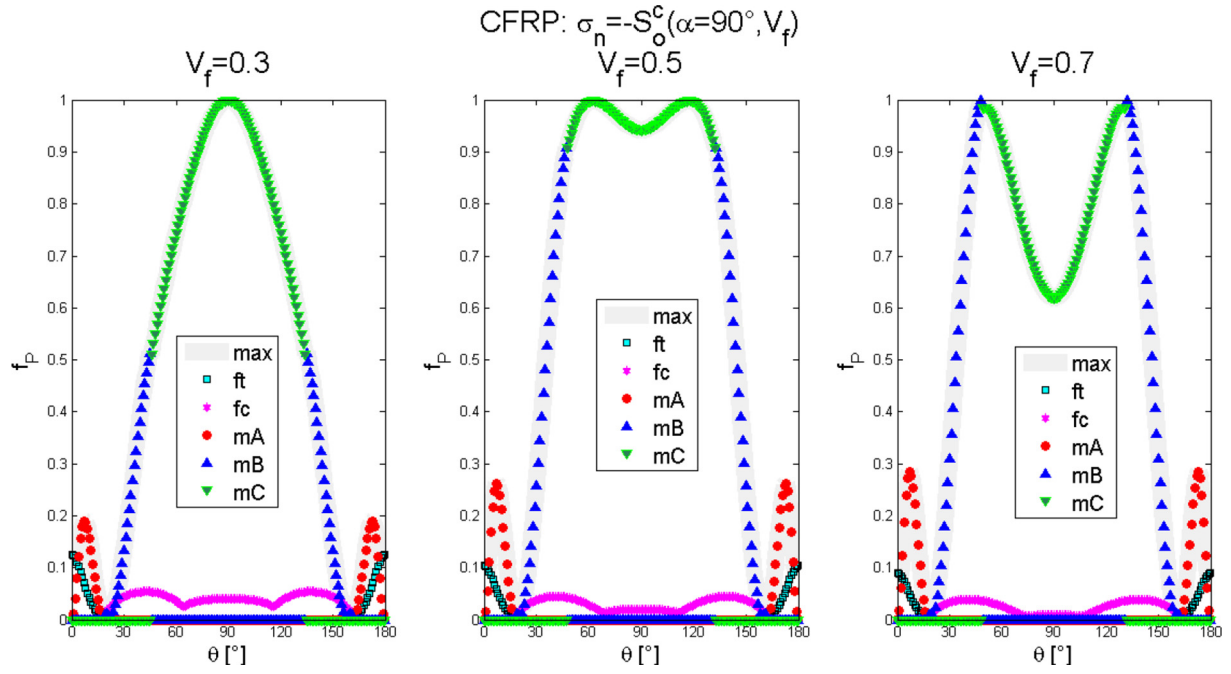
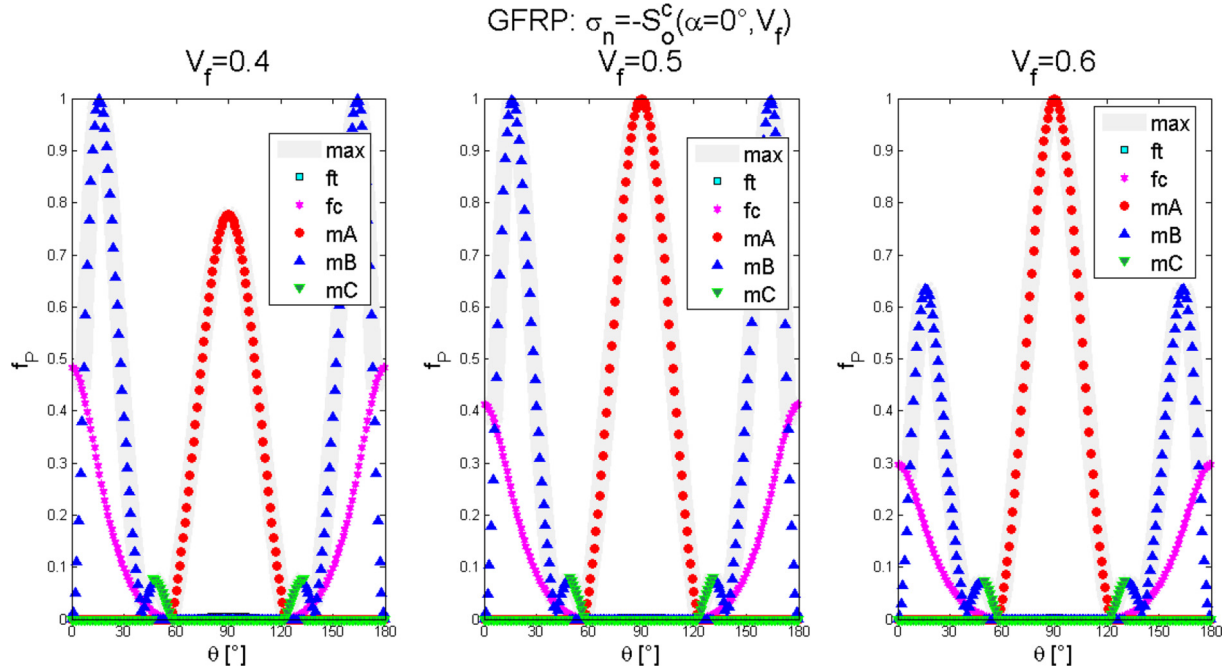**Fig. 15.** Influence of V_f on failure mode for CFRP with compressive load $\sigma_n = -S_o^c(\alpha = 90°, V_f)$.

Fig. 16. Influence of V_f on failure mode for GFRP with compressive load $\sigma_n = -S_o^c(\alpha = 0°, V_f)$.

Appendix A. Chamis model

Chamis model [13,46] estimates elastic properties based on the rule of mixtures. Essentially, the model alters the rule of mixtures by considering nonlinear influence of fiber volume fraction V_f. Changes are related to the transversal properties, replacing fiber volume fraction by $\sqrt{V_f}$. Hence, equations for the equivalent properties are given by

$$E_1 = E_1^f V_f + (1 - V_f)E^m \tag{A.1}$$

$$\nu_{12} = \nu_{12}^f V_f + (1 - V_f)\nu^m \tag{A.2}$$

$$E_2 = \frac{E_2^f E^m}{E_2^f(1 - \sqrt{V_f}) + E^m \sqrt{V_f}} \tag{A.3}$$

$$G_{12} = \frac{G_{12}^f G^m}{G_{12}^f(1 - \sqrt{V_f}) + G^m \sqrt{V_f}} \tag{A.4}$$

Tensile longitudinal strength is modeled based on the fiber maximum normal stress. On the other hand, compression strength is based on the fiber crushing, inter-ply delamination and fiber micro-buckling.
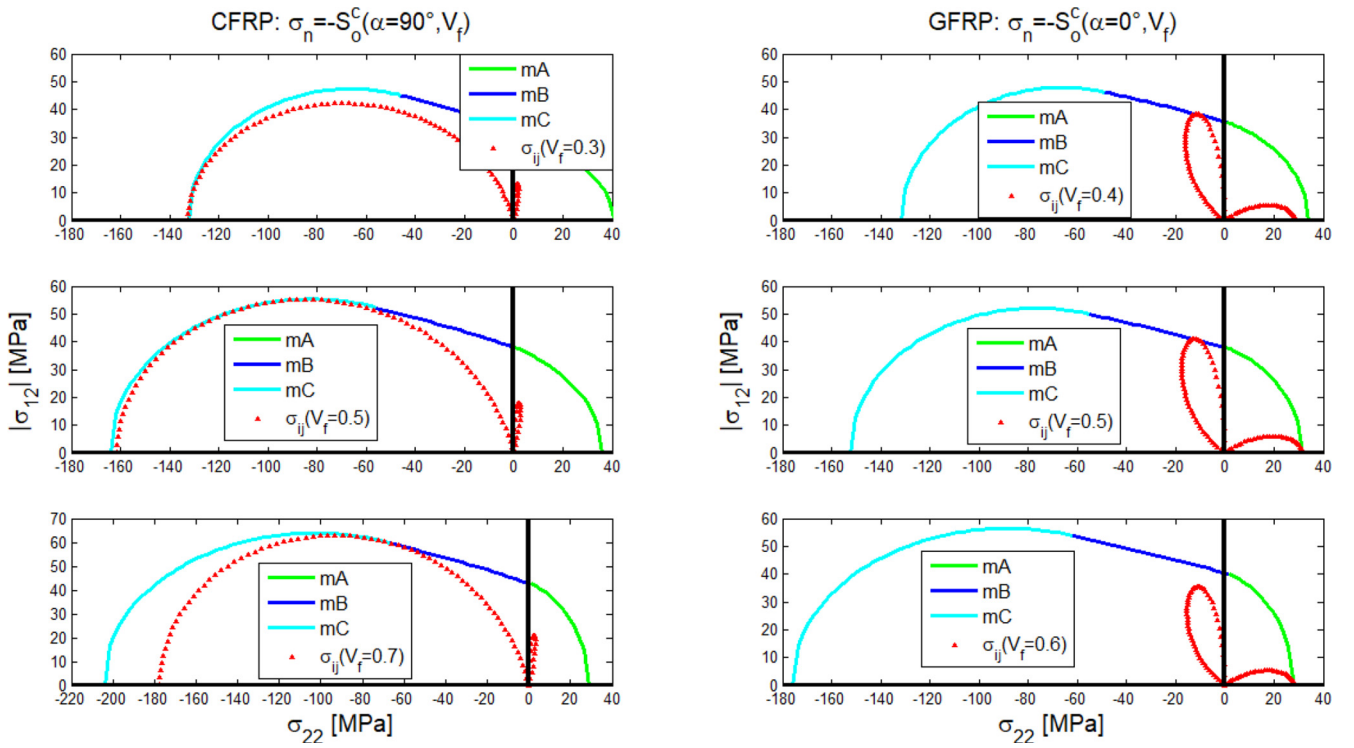
Fig. 17. Matrix failure envelopes in plane $\sigma_{12} - \sigma_{22}$ for CFRP with $\sigma_n = -S_o^c(\alpha = 90°, V_f)$ and GFRP with $\sigma_n = -S_o^c(\alpha = 90°, V_f)$.
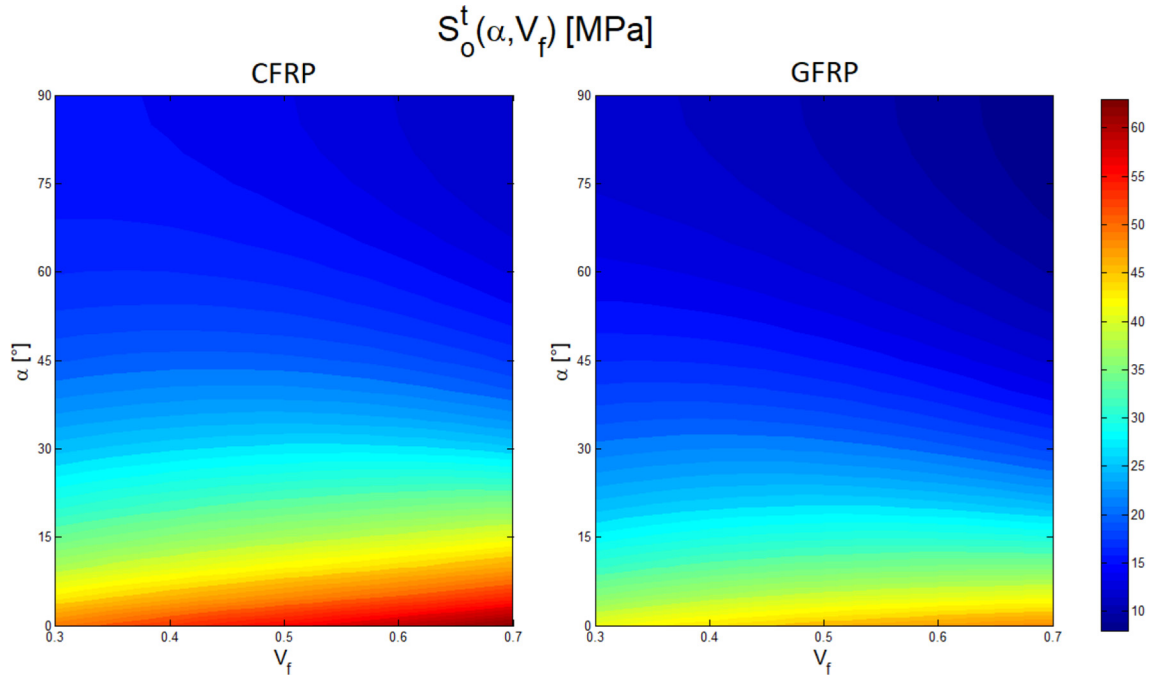

Fig. 18. Notched tensile strength, S_o^t, vs. α and V_f.

Concerning transversal and shear strengths, matrix failure is assumed to be preponderant. Under these assumptions, strengths are expressed by the following expressions:

$$S_{11}^t = \left[V_f + (1 - V_f) \left(\frac{E^m}{E_1^f} \right) \right] S_t^f \tag{A.5}$$

$$S_{11}^c = \min \left\{ \left[V_f + (1 - V_f) \left(\frac{E^m}{E_1^f} \right) \right] S_c^f, 10 S_{12}^s + 2.5 S_s^m, \frac{G^m}{1 - V_f \left(1 - \frac{G^m}{G_{12}^f} \right)} \right\} \tag{A.6}$$
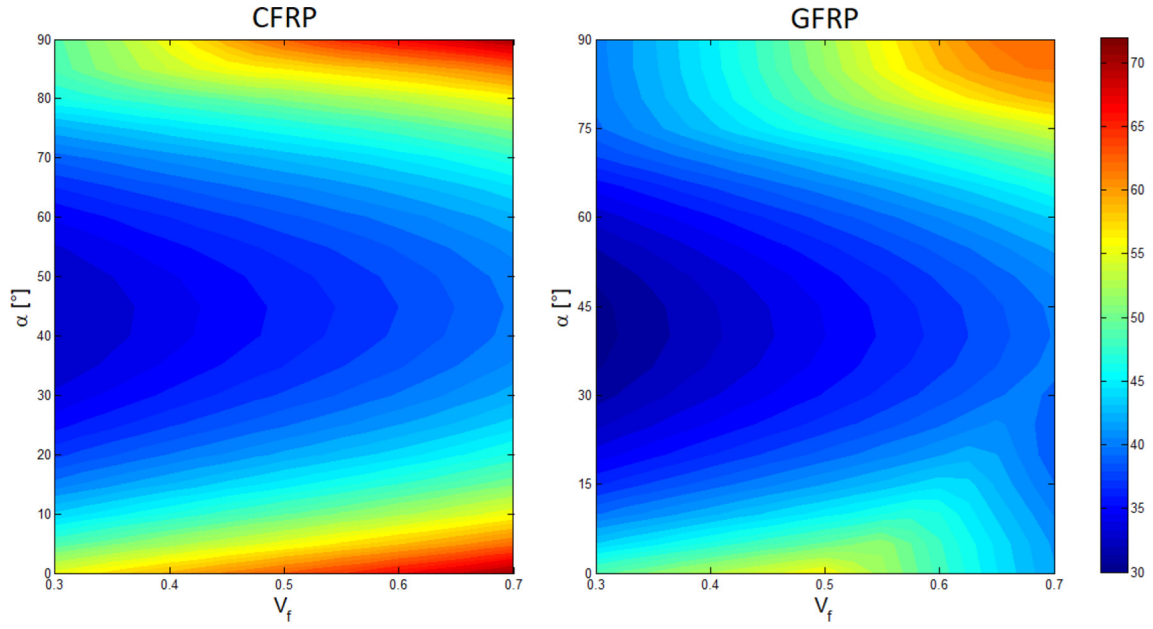
Fig. 19. Notched compressive strength, S_o^c, vs. α and V_f.

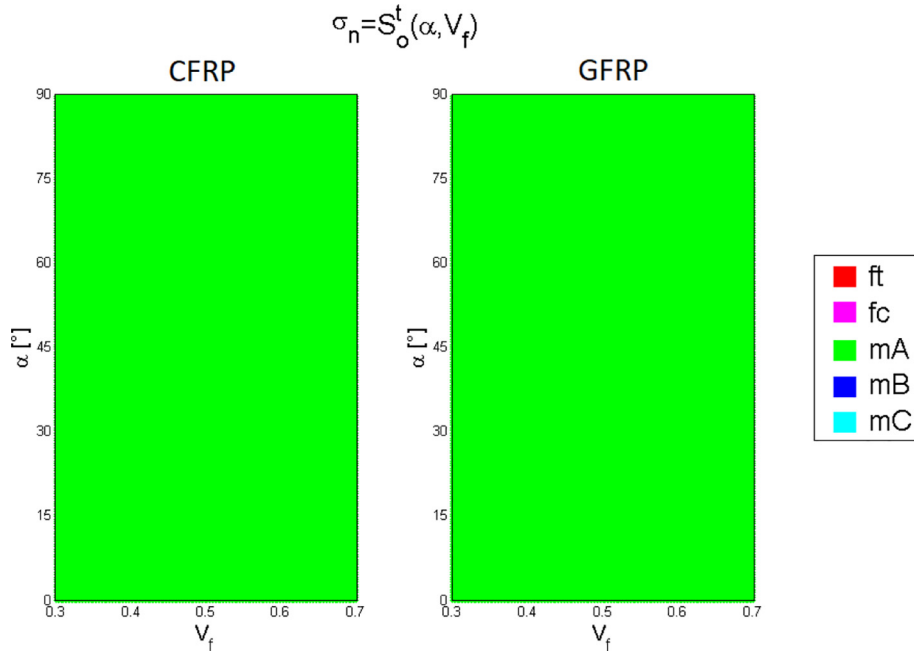**Fig. 20.** Change of failure mechanism for $\sigma_n = S_o^t$, vs. α and V_f.

$$S_{22}^t = \left[1 - \left(\sqrt{V_f} - V_f\right)\left(1 - \frac{E^m}{E_2^f}\right)\right]S_t^m \tag{A.7}$$

$$S_{22}^c = \left[1 - \left(\sqrt{V_f} - V_f\right)\left(1 - \frac{E^m}{E_2^f}\right)\right]S_c^m \tag{A.8}$$

$$S_{12}^s = \left[1 - \left(\sqrt{V_f} - V_f\right)\left(1 - \frac{G^m}{G_{12}^f}\right)\right]S_s^m \tag{A.9}$$

Appendix B. Bridging model

Bridging model [47] was first developed using the Mori-Tanaka model [48,49] and later was advanced using the concentric cylinders model [50]. Bridging model defines a correlation between matrix and fiber stress tensors using a fourth-order bridging tensor A_{ijkl}, written as follows:

$$\sigma_{ij}^m = A_{ijkl}\sigma_{kl}^f \tag{B.1}$$
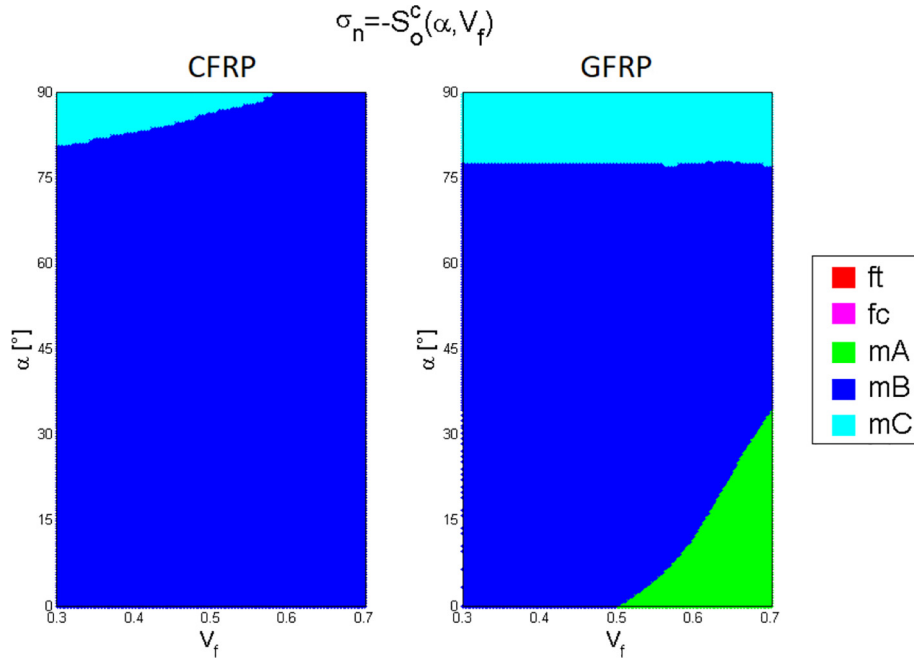
$$\sigma_n = -S_o^c(\alpha, V_f)$$

Fig. 21. Change of failure mechanism for $\sigma_n = -S_o^c$ vs. α and V_f.

The composite effective constitutive relation, $\sigma_{ij} = c_{ijkl}\varepsilon_{kl}$, can be obtained defining the stiffness tensor as

$$c_{ijkl} = [(1 - V_f)A_{ijpq} + V_f I_{ijpq}]D_{pqkl}^{-1} \tag{B.2}$$

where $D_{ijkl} = (1 - V_f)s_{ijpq}^m A_{pqkl} + V_f s_{ijkl}^f$ and the matrix and fibers compliance tensors s_{ijkl}^m and s_{ijkl}^f are the inverse to the stiffness tensors c_{ijkl}^m and c_{ijkl}^f, respectively.

Using the contracted notation to represent a fourth-order tensor as a 6×6 matrix, the bridging tensor non-zero components are given by [50]

$$[A]_{11} = \frac{E^m}{E_1^f}\left[1 + \frac{\nu^m(\nu^m - \nu_{12}^f)}{(1 + \nu^m)(1 - \nu^m)}\right] \tag{B.3}$$

$$[A]_{12} = [A]_{13} = \frac{1}{(1 - \nu^m)}\left\{\frac{E^m}{(1 + \nu^m)}\left[\frac{\nu^m(1 - \nu_{23}^f)}{2E_2^f} - \frac{\nu_{12}^f}{E_1^f}\right] + \frac{\nu^m}{2}\right\} \tag{B.4}$$

$$[A]_{21} = [A]_{31} = \frac{E^m}{2E_1^f}\frac{(\nu^m - \nu_{12}^f)}{(1 + \nu^m)(1 - \nu^m)} \tag{B.5}$$

$$\begin{aligned}[A]_{22} &= [A]_{33} \\ &= \frac{1}{(\nu^m - 1)(\nu^m + 1)}\left\{E^m\left[\frac{(\nu_{23}^f - 3)}{8E_2^f} + \frac{\nu^m\nu_{12}^f}{2E_1^f}\right] + \frac{(\nu^m + 1)(4\nu^m - 5)}{8}\right\}\end{aligned} \tag{B.6}$$

$$\begin{aligned}[A]_{32} &= [A]_{23} \\ &= \frac{1}{(1 - \nu^m)(1 + \nu^m)}\left\{E^m\left[\frac{(3\nu_{23}^f - 1)}{8E_2^f} + \frac{\nu^m\nu_{12}^f}{2E_1^f}\right] + \frac{(\nu^m + 1)(1 - 4\nu^m)}{8}\right\}\end{aligned} \tag{B.7}$$

$$[A]_{44} = \frac{G^m}{4G_{23}^f(1 - \nu^m)} + \frac{(3 - 4\nu^m)}{4(1 - \nu^m)} \tag{B.8}$$

$$[A]_{55} = [A]_{66} = \frac{G^m + G_{12}^f}{2G_{12}^f} \tag{B.9}$$

Composite strength properties according to the Bridging model are expressed as follows [51,52]:

$$S_{11}^t = \left[V_f + (1 - V_f)\left(\frac{E^m}{E_1^f}\right)\right]S_t^f \tag{B.10}$$

$$S_{11}^c = \left[V_f + (1 - V_f)\left(\frac{E^m}{E_1^f}\right)\right]S_c^f \tag{B.11}$$

$$S_{22}^t = \left[V_f\frac{E_{22}^f}{(\beta E_2^f + (1 - \beta)E^m)} + (1 - V_f)\right]\frac{S_t^m}{K_{22}^t} \tag{B.12}$$

$$S_{22}^c = \left[V_f\frac{E_{22}^f}{(\beta E_2^f + (1 - \beta)E^m)} + (1 - V_f)\right]\frac{S_c^m}{K_{22}^c} \tag{B.13}$$

$$S_{12}^s = \frac{S_s^m}{K_{12}\lambda_4} \tag{B.14}$$

where $\beta = 0.4$ is defined to fit the model with experimental results and

$$\begin{aligned}K_{22}(\varphi) &= \{1 + \tfrac{a}{2}\sqrt{V_f}\cos(2\varphi) + \tfrac{b}{2(1-\sqrt{V_f})}[V_f^2\cos(4\varphi) + 4(1 - 2\cos(2\varphi))V_f\cos^2(\varphi)] \\ &\quad + \sqrt{V_f}(2\cos(2\varphi) + \cos(4\varphi))\}\frac{V_f E_2^f + (1 - V_f)[\beta E_2^f + (1-\beta)E^m]}{\beta E_2^f + (1-\beta)E^m}\end{aligned} \tag{B.15}$$

$$K_{22}^t = K_{22}(0) \tag{B.16}$$

$$K_{22}^c = k_{22}(\phi) \tag{B.17}$$

$$\phi = \frac{\pi}{4} + \frac{1}{2}a\sin\left(\frac{S_c^m - S_t^m}{S_c^m + S_t^m}\right) \tag{B.18}$$

$$a = \frac{[1 - \nu^m - 2(\nu^m)^2]E_2^f - [1 - \nu_{23}^f - 2(\nu_{23}^f)^2]E^m}{(1 + \nu^m)E_2^f + [1 - \nu_{23}^f - 2(\nu_{23}^f)^2]E^m} \tag{B.19}$$

$$b = \frac{(1 + \nu_{23}^f)E^m - (1 + \nu^m)E_2^f}{[\nu^m + 4(\nu^m)^2 - 3]E_2^f - (1 + \nu_{23}^f)E^m} \tag{B.20}$$

$$K_{12} = \left[1 - V_f\left(\frac{G_{12}^f - G^m}{G_{12}^f + G^m}\right)\left(W - \frac{1}{3}\right)\right]\frac{[V_f + a_{66}(1 - V_f)]}{a_{66}} \quad (B.21)$$

$$W = \pi\sqrt{V_f}\left(\frac{1}{4V_f} - \frac{4}{128} - \frac{2}{512}V_f - \frac{5}{4096}V_f^2\right) \quad (B.22)$$

$$\lambda_4 = \frac{a_{66}}{V_f + a_{66}(1 - V_f)} \quad (B.23)$$

$$a_{66} = 0.3 + 0.7(G^m/G_{12}^f) \quad (B.24)$$

References

[1] Kalamkarov AL. Asymptotic homogenization method and micromechanical models for composite materials and thin-walled composite structures, Mathematical Methods and Models in Composites, Imperial College Press, London, UK, 2014, pp. 1–60.

[2] Tsai SW, Melo JDD. An invariant-based theory of composites. Compos Sci Technol 2014;100:237–43.

[3] Kaddour AS, Hinton MJ, Smith PA, Li S. The background to the third world-wide failure exercise. J Compos Mater 2013;47:2417–26.

[4] Soden PD, Kaddour AS, Hinton MJ. Recommendations for designers and researchers resulting from the world-wide failure exercise. Comp Sci Technol 2004;64:589–604.

[5] Kaddour AS, Hinton MJ. Maturity of 3D failure criteria for fibre reinforced composites: comparison between theories and experiments: Part B of WWFE-II. J Compos Mater 2013;47:925–66.

[6] Kalamkarov AL, Kolpakov AG. Analysis, design and optimization of composite structures. 2nd ed. Chichester, NY: Wiley; 1997.

[7] Benveniste Y. A new approach to the application of Moti-Tanaka's theory in composite materials. Mech Mater 1987;6:147–57.

[8] Hashin Z. Thermoelastic properties of fiber composites with imperfect interface. Mech Mater 1990;8:333–48.

[9] Christensen RM. Mechanics of composite materials. New York: Dover Publications; 2005.

[10] Bravo-Castillero J, Guinovart-Díaz R, Rodríguez-Ramos R, Sabina FJ, Brenner R. Unified analytical formulae for the effective properties of periodic fibrous composites. Mater Lett 2012;73:68–71.

[11] Carrere N, Laurin F, Maire JF. Micromechanical-based hybrid mesoscopic 3D approach for non-linear progressive failure analysis of composite structures. J Compos Mater 2012;46:2389–415.

[12] Macedo RQ, Ferreira RTL, Guedes JM, Donadon MV. Intraply failure criterion for unidirectional fiber reinforced composites by means of asymptotic homogenization. Compos Struct 2017;159:335–49.

[13] Chamis CC, Abdi F, Garg M, Minnetyan L, Baid H, Huang D, et al. Micromechanics-based progressive failure analysis prediction for WWFE-III composite coupon test cases. J Compos Mater 2013;47:2695–712.

[14] Huang ZM, Liu L. Predicting strength of fibrous laminates under triaxial loads only upon independently measured constituent properties. Int J Mech Sci 2014;79:105–29.

[15] Andrianov IV, Awrejcewicz J, Danishevs'kyy VV. Asymptotical Mechanics of Composites – Modelling Composites without FEM, Springer, 2018.

[16] Savin GN. Stress Distribution Around Holes, NASA Technical Translation, Washington, D.C., 1970.

[17] Lekhnitskii SG. Anisotropic plates. 3rd ed. Gordon and Breach Sc. Publ, NY; 1987.

[18] Hwu C, Ting TCT. Two-dimensional problems of the anisotropic elastic solid with an elliptic inclusion. Q J Mech Appl Math 1989;42:553–72.

[19] Ting TCT. Anisotropic elasticity: theory and applications. New York: Oxford University Press; 1996.

[20] Hwu C. Anisotropic elastic plates. NY: Springer; 2009.

[21] Tan SC. Laminated composites containing an elliptical opening. I. Approximate stress analyses and fracture models. J. Compos. Mater. 1987;21:925–48.

[22] Kaman MO. Effect of fiber orientation on fracture toughness of laminated composite plates $[0/\theta]s$. Eng Fract Mech 2011;78:2521–34.

[23] Vignoli LL, Castro JTP. A parametric study of stress concentration issues in unidirectional laminates. Mech Adv Mater Struct 2020. in press.

[24] Iarve EV, Mollenhauer D, Kim R. Theoretical and experimental investigation of stress redistribution in open hole composite laminates due to damage accumulation. Compos Part A-Appl. S 2005;36:163–71.

[25] Mollenhauer D, Iarve EV, Kim R, Langley B. Examination of ply cracking in composite laminates with open holes: a moiré interferometric and numerical study. Compos Part A-Appl S 2006;37:282–94.

[26] Lee J, Soutis C. Measuring the notched compressive strength of composite laminates: specimen size effects. Compos Sci Technol 2008;68:2359–66.

[27] O'Higgins RM, McCarthy MA, McCarthy CT. Comparison of open hole tension characteristics of high strength glass and carbon fibre-reinforced composite. Compos Sci Technol 2008;68:2770–8.

[28] Shah PD, Melo JDD, Cimini Jr CA, Ridha M. Evaluation of notched strength of composite laminates for structural design. J Compos Mater 2010;44:2381–92.

[29] Vignoli LL, Castro JTP, Meggiolaro MA. Stress concentration issues in unidirectional laminates. J Braz Soc Mech Sci Eng 2019;41:462.

[30] Vignoli LL, Savi MA, Pacheco PMCL, Kalamkarov AL. Comparative analysis of micromechanical models for the elastic composite laminae. Compos Part B Eng 2019;174:. https://doi.org/10.1016/j.compositesb.2019.106961106961.

[31] Vignoli LL, Savi MA, Pacheco PMCL, Kalamkarov AL. Micromechanical analysis of transversal strength of composite laminae. Compos Struct 2020;250:. https://doi.org/10.1016/j.compstruct.2020.112546112546.

[32] Vignoli LL, Savi MA, Pacheco PMCL, Kalamkarov AL. Micromechanical analysis of longitudinal and shear strength of composite laminae. J Compos Mater 2020. https://doi.org/10.1177/0021998320936343.

[33] Ramos RR, Medeiros R, Díaz RG, Castillero JB, Otero JA, Tita V. Different approaches for calculating the effective elastic properties in composite materials under imperfect contact adherence. Compos Struct 2013;99:264–75.

[34] Barbero EJ. Introduction to composite materials design. 3rd ed.,. CRC Press; 2018.

[35] Puck A, Schurmann H. Failure analysis of FRP laminates by means of physically based phenomenological models. Compos Sci Technol 1998;58:1045–67.

[36] Knops M. Analysis of failure in fiber polymer laminates: the theory of Alfred Puck. Leipzig: Springer; 2008.

[37] ASTM D3518/D3518M – 18, Standard Test Method for In-Plane Shear Response of Polymer Matrix Composite Materials by Tensile Test of a ±45° Laminate.

[38] Kaddour AS, Hinton MJ. Input data for test cases used in benchmarking triaxial failure theories of composites. J Compos Mater 2012;46:2295–312.

[39] Góes RCO, Castro JTP, Meggiolaro MA. 3D thickness effects around notch and crack tips. Int J Fatigue 2014;62:159–70.

[40] ASTM D5766/D5766M – 11, Standard Test Method for Open-Hole Tensile Strength of Polymer Matrix Composite Laminates.

[41] ASTM D6484/D6484M – 14, Standard Test Method for Open-Hole Compressive Strength of Polymer Matrix Composite Laminates.

[42] Hart-Smith LJ. Expanding the capabilities of the Ten-Percent Rule for predicting the strength of fibre-polymer composites. Compos Sci Technol 2002;62:1515–44.

[43] Tsai SW, Sharma N, Arteiro A, Roy S, Rainsberger B. Composite grid/skin structures – low weight/low cost design and manufacturing, Stanford University, 2019.

[44] Griffith AA. The phenomena of rupture and flow in solids. Philos Trans Roy Soc London 1921;A221:163–98.

[45] Castro JTP, Meggiolaro MA. Fatigue design techniques: vol. I – High-cycle fatigue. CreateSpace Independent Publishing Platform 2016.

[46] Chamis CC. Mechanics of composite materials: past, present, and future. J Compos Tech Res 1989;11:3–14.

[47] Huang ZM, Zhou YX. Strength of fibrous composites. Springer; 2011.

[48] Huang ZM. A unified micromechanical model for the mechanical properties of two constituent composite materials. Part I: elastic behavior. J Thermoplast Compos Mater 2000;13:252–71.

[49] Huang ZM. A unified micromechanical model for the mechanical properties of two constituent composite materials Part III: strength behavior. J Thermoplast Compos Mater 2001;14:54–69.

[50] Wang YC, Huang ZM. A New Approach to a Bridging Tensor, 2015;36:1417–31.

[51] Huang ZM, Xin LM. In situ strengths of matrix in a composite. Acta Mech Sin 2017;33:120–31.

[52] Huang ZM. On micromechanics approach to stiffness and strength of unidirectional composites. J Reinf Plast Compos 2019;38:167–96.